Nanoscale

PAPER

View Journal | View Issue

Cite this: *Nanoscale*, 2015, **7**, 17012

$Pd_2Au_{36}(SR)_{24}$ cluster: structure studies†

Bei Zhang,[a] Sameh Kaziz,[b] Houhua Li,[c] Dawid Wodka,[a] Sami Malola,[d] Olga Safonova,[e] Maarten Nachtegaal,[e] Clément Mazet,[c] Igor Dolamic,[a] Jordi Llorca,[f] Elina Kalenius,[g] Latévi Max Lawson Daku,[a] Hannu Hakkinen,[d,g] Thomas Bürgi*[a] and Noelia Barrabés*‡[a]

Received 29th June 2015,
Accepted 14th September 2015

DOI: 10.1039/c5nr04324g

www.rsc.org/nanoscale

The location of the Pd atoms in $Pd_2Au_{36}(SC_2H_4Ph)_{24}$, is studied both experimentally and theoretically. X-ray photoelectron spectroscopy (XPS) indicates oxidized Pd atoms. Palladium K-edge extended X-ray absorption fine-structure (EXAFS) data clearly show Pd–S bonds, which is supported by far infrared spectroscopy and by comparing theoretical EXAFS spectra in R space and circular dichroism spectra of the staple, surface and core doped structures with experimental spectra.

Introduction

Interest in atomically precise and well defined gold nanoclusters ($Au_n(SR)_m$) has greatly increased in recent years, due to their unique size-specific physical and chemical properties.[1] These clusters typically consist of a symmetric metal core protected by multiple gold-thiolate staples –SR–(Au–SR–)$_n$ (n = 1, 2). Recent studies furthermore showed even longer staples such as $Au_3(SR)_4$,[2] $Au_4(SR)_5$ [3] or $Au_5(SR)_6$.[4] Extended studies have been performed focusing on the synthesis, characterization and properties of these gold nanostructures. Particularly stable clusters were found to be $Au_{25}(SR)_{18}$,[5,6] $Au_{38}(SR)_{24}$,[7] $Au_{40}(SR)_{24}$,[8,9] $Au_{102}(SR)_{44}$,[10] and $Au_{144}(SR)_{60}$,[11] although later a large number of stable clusters has been found (see examples in ref. 12–18 and in the recent book devoted to this field[19]).

Recently heteroatom doping of gold nanoclusters has been introduced,[20,21] which represents a viable strategy to study the sensitivity of physical-chemical properties of the nanoclusters towards replacement of a single or few gold atoms by other metals.[21–24] Furthermore, it provided the possibility of fine-tuning the properties of these $Au_n(SR)_m$ clusters.[24–29] Several well-defined bimetallic clusters have been studied recently with single or multiple doping atoms (Pd,[20,30–33] Pt,[26] Cu,[24,34–36] Ag,[23,36–38] Mn[39]).

Application of these doped-thiolate gold nanoclusters requires the understanding of the atomic structure and determination of the exact position of the foreign (dopant) atoms. Highly selective synthesis protocols or separation techniques are critical in order to obtain high purity samples of the metal clusters for structure studies.[40] In addition to these challenges, it is also difficult to obtain single crystals of the atomic precise doped gold nanoclusters to confirm the dopant location by XRD. Few crystals of doped gold nanoclusters ($Au_{25-x}M_x(SR)_{18}$, M: Cd, Cu, Ag, x = 1–13, $Au_{12}Ag_{32}(SR)_{30}$ and $[Au_{12+n}Cu_{32}(SR)_{30+n}]^{4-}$) have been obtained.[37,41–46] Furthermore, the crystallization process may favour certain structures of a mixture thus biasing the structure determination. Experimentally, mass spectrometry (MS) and extended X-ray absorption fine structure analysis (EXAFS) are powerful alternatives to study the composition and local geometric structure of doped nanoclusters respectively without the need to crystallize the samples.[36,47,48] Structures of the parent thiolate protected gold clusters ($Au_{25}(SR)_{18}$,[49] $Au_{38}(SR)_{24}$ [7] and $Au_{102}(SR)_{44}$ [50]) have been confirmed by X-ray crystallography. With respect to the respective doped clusters, which are thought to have structures analogous to the parent gold clusters, the most intriguing question is the dopant location. The most extensively studied clusters so far are doped $Au_{25}(SR)_{18}$ nanoclusters, which have three principle possible dopant positions: (1) in the staples; (2) in the icosahedral shell; and (3) in the center site. EXAFS analysis support the center dopant location of monodoped $PdAu_{24}(SR)_{18}$ [30] and $PtAu_{24}(SR)_{18}$ [51,52] clusters, which are also

[a]*Department of Physical Chemistry, University of Geneva, 30 Quai Ernest-Ansermet, 1211 Geneva 4, Switzerland. E-mail: noe.barrabes@gmail.com*
[b]*Department of Industrial Engineering, National High School of Engineers of Tunis, Tunis, Tunisia*
[c]*Department of Organic Chemistry, University of Geneva, 30 Quai Ernest-Ansermet, 1211 Geneva 4, Switzerland*
[d]*Department of Physics, Nanoscience Center, University of Jyväskylä, FI-40014 Jyväskylä, Finland*
[e]*Paul Scherrer Institute, 5232 Villigen, Switzerland*
[f]*Institute of Energy Technologies and Centre for Research in NanoEngineering, Technical University of Catalonia, Barcelona, Spain*
[g]*Department of Chemistry, Nanoscience Center, University of Jyväskylä, FI-40014 Jyväskylä, Finland*

†Electronic supplementary information (ESI) available: The experimental part (synthesis and characterization). Additional MALDI, ESI, UV-vis, CD measurements and DFT calculations, EXAFS simulation results described in the text. See DOI: 10.1039/c5nr04324g

‡N.B. new address is Institute of Materials Chemistry, Technical University of Vienna, Getreidemarkt 9/BC/01. 1060 Vienna (Austria)

computationally the most stable. In multi-doped $Au_{25}(SR)_{18}$ clusters, $Ag_xAu_{25-x}(SR)_{18}$ and $Cu_xAu_{25-x}(SR)_{18}$, only a mixture (different x) could be isolated. For clusters with high mixing ratio x, $Ag_xAu_{25-x}(SR)_{18}$ ($x \leq 13$) and $Cu_xAu_{25-x}(SR)_{18}$ ($x \leq 5$), Dass,[37] Jin[53] and Negishi[24] reported that the dopant preferentially occupied the shell of the icosahedral core. Nevertheless, when the mixing ratio is reduced, Cu atoms are confirmed by EXAFS to be at the theoretically less favored staple sites of $Cu_xAu_{25-x}(SR)_{18}$ ($x \approx 1$) due to stabilization of Cu at these positions in oxidative synthesis and storage condition.[36]

$Au_{38}(SC_2H_4Ph)_{24}$ nanocluster has received particular interest for its well-defined structure and intrinsic chirality.[54] It comprises a bi-icosahedral Au_{23} core, three monomeric and six dimeric protecting staples.[7] Negishi *et al.* performed the synthesis and isolation of $Pd_2Au_{36}(SC_2H_4Ph)_{24}$ nanocluster by Size Exclusion Chromatography and preferential decomposition of side products.[32] The doped cluster gives rise to higher stability compared to $Au_{38}(SC_2H_4Ph)_{24}$ against decomposition in THF. The structure in which the two Pd atoms are located in the center of the icosahedron is computationally most stable structure. However, no direct experimental analysis has been reported so far to support the center doped structure. Our group recently reported the enantioseparation of $Pd_2Au_{36}(SC_2H_4Ph)_{24}$ clusters.[33] Compared to $Au_{38}(SR)_{24}$, Pd doping significantly changed the features in the circular dichroism spectrum. The doped cluster showed racemization at lower temperature, indicating a more flexible Au–S interface.

In this contribution we study the location of the Pd dopant in atomic precise $Pd_2Au_{36}(SC_2H_4Ph)_{24}$ nanocluster. A series of size exclusion chromatography (SEC) and high performance liquid chromatography (HPLC) separations have been performed to isolate the doped cluster. New staple vibrations in the far infrared (FIR) spectra and oxidized Pd in X-ray photoelectron spectroscopy (XPS) indicate Pd–S bonds. The location of Pd atoms in $Pd_2Au_{36}(SC_2H_4Ph)_{24}$ was further studied by density functional theory (DFT) calculations and Pd K-edge EXAFS. We performed geometry optimization, UV and circular dichroism (CD) spectra calculation and EXAFS fitting for three structures with the two Pd atoms doped inside the Au_{38} core, on the core surface or in the staples. DFT calculations predicted that doping inside the core is much more stable. However, both time-dependent density functional theory (TDDFT) calculations of the CD spectra and EXAFS fitting suggested that the calculated center doped structure and long staple doped structure contributed to the experimental data. EXAFS fitting suggested a mixture of 46% core doped structure and 54% staple doped structure in the $Pd_2Au_{36}(SC_2H_4Ph)_{24}$ sample.

Experimental

Synthesis and isolation of $Pd_2Au_{36}(SC_2H_4Ph)_{24}$ clusters

The synthesis and separation procedure in order to obtain highly pure palladium doped cluster was described in our previous work.[33] Briefly, $Pd_xAu_{38-x}(SR)_{24}$ (x = 1, 2) clusters were synthesized following an adapted protocol based on the work of Negishi *et al.*[32] The main difference to the previous synthesis concerns the purification steps. After extraction of the crude product with acetonitrile (separation of $PdAu_{24}(SC_2H_4Ph)_{18}$ clusters), a second extraction with acetone is performed in order to completely remove $Au_{25}(SC_2H_4Ph)_{18}$. Then the nanoclusters were isolated in a gel permeation column (GPC/SEC)[4] followed by HPLC separation steps, till the collected samples showed only the signal of $[Pd_2Au_{36}(SC_2H_4Ph)_{24}]^-$ in the matrix-assisted laser desorption ionization mass spectrometry (MALDI-TOF) analysis.

UV–vis spectra were recorded on a Varian Cary 50 spectrometer. Quartz cuvettes of 10 or 5 mm path length were used (solvents: methylene chloride and toluene). MALDI-TOF mass spectra were obtained on a Shimadzu Biotech Axima mass spectrometer in linear mode. DCTB was used as matrix (see ESI† for synthesis description and characterization of the pure sample).

Positive-mode electrospray ionization mass spectrometry (ESI) measurements

ESI mass spectra were acquired on ESI-qTOF QSTAR Elite equipped with an API 200 TurboIonSpray ESI source (ABSciex). A 0.4 mM toluene solution of $Pd_2Au_{36}(SC_2H_4Ph)_{24}$ was prepared. To this solution, stock solution of cesium acetate (5 μL of 50 mM CsOAc in methanol) and additional methanol were added to obtain a final sample concentration of 188 μM. The solution was infused into the ESI source at a flow rate of 5 μL min^{-1}. The parameters were optimized to get maximum abundance of the ions under study. Room-temperature nitrogen was used as nebulization (25 psi) and as curtain gas (18 psi). The ion-source voltages of 5.5 kV for capillary, 225 V for the oriface plate (declustering potential), 5 V as potential difference between skimmer and pre-quadrupole, and 250 V for the potential difference between the focusing ring and pre-quadrupole were used. Accumulation delay of 3 s, ion release delay of 6 ms and ion release width of 5 ms were used. Each spectrum was an average of spectra collected within 5 min, each of these containing 40 individual scans that were averaged before being sent from the instrument to data system. The measurement and data handling was accomplished with Analyst® QS 2.0 Software. Mass spectra were externally calibrated by using ESI Tuning mix (Agilent Technologies). The monoisotopic resolution was not obtained, but the charge states of the ions were determined by characteristic Cs^+ mass differences and by comparison of the peak shape to the shape of theoretic isotopic distributions. The compositions of the ions were finally verified by comparing experimental m/z values with the theoretical ones.

High resolution transmission electron microscopy (HRTEM) measurements

Microstructural characterization by High Resolution Transmission Electron Microscopy (HRTEM) was performed at an accelerating voltage of 200 kV in a JEOL 2010F instrument equipped with a field emission source. The point-to-point resolution was 0.19 nm and the resolution between lines was

0.14 nm. Samples were dispersed in toluene in an ultrasonic bath. Images were not filtered or treated by means of digital processing, and they correspond to raw data. A minimum of 300 particles were measured in each sample for particle size determination. The size limit for the detection of nanoparticles was about 0.8 nm. The average particle diameter was calculated from the mean diameter frequency distribution with the formula: $d = \sum n_i d_i / \sum n_i$, where n_i is the number of particles with particle diameter d_i in a certain range.

X-ray photoelectron spectroscopy (XPS) measurements

X-ray photoelectron spectroscopy (XPS) was done on a SPECS system equipped with an Al anode XR50 source operating at 150 mW and a Phoibos MCD-9 detector. The pressure in the analysis chamber was always below 10^{-7} Pa. The pass energy of the hemispherical analyzer was set at 25 eV and the energy step was set at 0.1 eV. Samples were dissolved in toluene and drop-casted directly over the sample holder. Data processing was performed with the CasaXPS program (Casa Software Ltd, UK). The binding energy (BE) values were referred to the C 1s peak at 284.8 eV. Atomic fractions (%) were calculated using peak areas normalized on the basis of acquisition parameters after background subtraction, experimental sensitivity factors and transmission factors provided by the manufacturer. Background subtraction was done with Shirley background.

Far infrared spectroscopy

FIR spectra were recorded on a Bruker Vertex 80sv Fourier transform IR spectrometer. Measurements were performed in vacuum at a resolution of 4 cm^{-1} by averaging 200 scans. A Mylar 6 mm multilayer beamsplitter was used. The samples were dissolved in dichloromethane, spread over a silicon window substrate and dried.

Calculations

Calculations were done with density-functional theory (DFT), real-space grid based projector-augmented wave code-package GPAW, that includes scalar-relativistic corrections for gold-setup.[55,56] Structural relaxation of staple, surface and core doped $Pd_2Au_{36}(SC_2H_4Ph)_{24}{}^{(-2)}$ clusters were done using 0.2 Å grid spacing, 0.05 eV $Å^{-1}$ convergence criterion for maximum forces acting on atoms, and local density approximation (LDA) xc-functional.[57] Optical absorption and CD spectra were calculated using Casida formulation of linear response time-dependent DFT (TDDFT), 0.25 Å grid spacing and PBE (Perdew–Burke–Enrzerhof) functional.[58–60]

X-ray absorption fine structure (XAFS) measurements and fitting approach

X-ray absorption fine structure (XAFS) measurements at the Pd K-edge (24.35 keV) were carried out at the Super-XAS beamline at the Swiss Light Source (Villigen, Switzerland). A solid sample of $Pd_2Au_{36}(SC_2H_4Ph)_{24}$ was dissolved in a small volume of dichloromethane and the concentrated solution was drop-cast onto scotch tape and dried. The spectra were measured in fluorescence mode using a five element silicon drift detector. The fitting procedure was performed by Ifeffit software suite.[61] The EXAFS spectra were background corrected and normalized, and the resulting k^2 weighted EXAFS spectra were Fourier transformed from 3–10 $Å^{-1}$. A two shell EXAFS (Pd–S and Pd–Au) fit was performed for the $Pd_2Au_{36}(SC_2H_4Ph)_{24}$ spectra. A FT-EXAFS window of 1 to 3.5 Å was used for the fitting. The $S_0{}^2$ was fixed at 0.86 (deduced from the fitting of the Pd foil). In each structure, all R-values were correlated and all other parameters (E_0 and σ^2) were allowed to run free, except coordination number (CN) that was fixed based on the theoretical calculations. The EXAFS data of $Pd_2Au_{36}(SC_2H_4Ph)_{24}$ were simulated based on the optimized structure from DFT calculations. The simulated data of each structure was the sum of all scattering paths generated by FEFF calculations. The location of the Pd dopant was determined by comparing the simulated EXAFS spectra with the experimental one. The EXAFS data of the staple doped and center doped mixture were fitted with 2 Pd–S scattering paths for the first structure and 12 Pd–Au scattering paths the second one. The molar ratio between the two structures was calculated accordingly.

Results and discussion

As described before,[33] the second enantiomer of $Pd_2Au_{36}(SC_2H_4Ph)_{24}$ (E2) can be obtained in high purity by chromatography separation, which was confirmed by MALDI, UV and CD studies (ESI†). In order to explore the cluster composition, ESI-MS analysis was performed. The positive-mode ESI spectrum in Fig. 1 shows three cationic species of $Pd_2Au_{36}(SC_2H_4Ph)_{24}$ by different number of Cs^+ cations attached. The most abundant peak with the m/z of 10 729.38 can be assigned to $[Pd_2Au_{36}(SC_2H_4Ph)_{24} + Cs]^+$, which indicates a neutral cluster. The theoretical isotopic distribution for that ion (red solid lines in Fig. S2†) is consistent with the

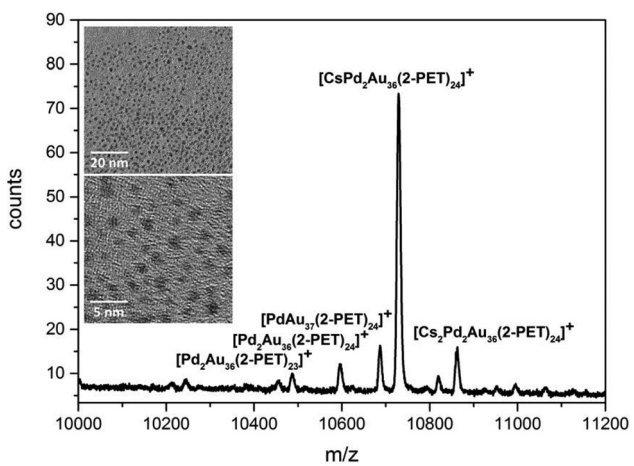

Fig. 1 Positive polarization ESI-MS spectrum of $Pd_2Au_{36}(SC_2H_4Ph)_{24}$. Inset: HRTEM image from $Pd_2Au_{36}(SC_2H_4Ph)_{24}$ sample.

experimental peak shape. The existence of 1− cluster charge was also shown as a minor peak at *m*/*z* value of 10 862.43, which is related to $[Pd_2Au_{36}(SC_2H_4Ph)_{24} + 2Cs]^+$. Small peaks for $[Pd_2Au_{36}(SC_2H_4Ph)_{24}]^+$ ion (*m*/*z* 10 596.88), $[Pd_2Au_{36}(SC_2H_4Ph)_{23} + Cs]^+$ ion (*m*/*z* 10 487.16) and $[PdAu_{37}(SC_2H_4Ph)_{24}]^+$ ion (*m*/*z* 10 687.14) could also be found. The only plausible electrochemical oxidation process in positive-mode ESI measurements ruled out the possibility of forming 1-cluster charge during the measurement.[62] This suggests there are some negative cluster charge state species in the $Pd_2Au_{36}(SC_2H_4Ph)_{24}$ sample.

The observation of neutral and +1 charge states may have several origins including: (1) oxidation of negatively charged species during ESI measurement, (2) presence of $Pd_2Au_{36}(SC_2H_4Ph)_{24}$ isomers with different Pd dopant locations in the sample.

Complementary high resolution transmission electron microscopy (HRTEM) studies confirmed the high homogeneity of the sample. A general view of $Pd_2Au_{36}(SC_2H_4Ph)_{24}$ clusters is shown in Fig. 1 inset. The distribution of particle size is very narrow and centered at about 0.9 nm (98% of all particles are within the range 0.8–1.1 nm). Particles are round-shaped and neither sharp edges nor well-defined lattice fringes are observed in the HRTEM images. The small size of the particles and the presence of the thiol ligands prevented any EDX or EELS analysis.

X-ray photoelectron spectroscopy (XPS) confirmed the presence of Pd and further gave information about its state. Fig. 2 shows de-convoluted XPS spectrum. There are two components for Au, the main one (337.7 eV and 355.7 eV) likely corresponds to oxidized Au (Au–SR interactions) and the other one (334.7 eV and 352.8 eV) can be ascribed to metallic Au from the cluster core (Table 1). With respect to Pd atoms, there is only one component at binding energies corresponding to oxidized Pd (336.8 eV and 342.1 eV). This is compatible with an interaction between Pd and a more electronegative element (for example, S). The peak at *ca.* 349 eV and 150 eV are assigned to a Ca impurity.

Table 1 XPS Compositional analysis of $Pd_2Au_{36}(SC_2H_4Ph)_{24}$

	Au_{red}		Au_{ox}		Pd_{ox}	
Binding energy (eV)	Au $4d_{5/2}$ 334.7	Au $4d_{3/2}$ 352.8	Au $4d_{5/2}$ 337.7	Au $4d_{3/2}$ 355.7	Pd $3d_{5/2}$ 336.8	Pd $3d_{3/2}$ 342.1
Atomic composition (%)	13.5		79.0		7.5	

The vibrational modes of the staples in the cluster surface should be altered if the Pd atoms are located in the staples. We therefore compared the FIR spectra of parent $Au_{38}(SC_2H_4Ph)_{24}$ and $Pd_2Au_{36}(SC_2H_4Ph)_{24}$ nanoclusters (Fig. 3). The two spectra are quite similar, showing that the basic structure of the staples is the same in both cases.[63] The bands at 217, 285 and 320 cm^{-1} in both nanoclusters can be assigned to radial, tangential/radial and tangential Au–S modes, respectively. Notably, a new bands at 160, 246 and 320 cm^{-1} was found in $Pd_2Au_{36}(SC_2H_4Ph)_{24}$ sample, which can be assigned to modes involving Pd–S bonds.[64] This indicates that at least a part of the Pd atoms is located in the staples, which is consistent with XPS that showed oxidized Pd. This is in contrast to the proposed center doped structure proposed based on DFT calculations,[32] in which both Pd atoms are inside the Au_{23} core. Further differences in the FTIR of $Pd_2Au_{36}(SC_2H_4Ph)_{24}$ and $Au_{38}(SC_2H_4Ph)_{24}$ concern the intensity of bands, such as at 180 cm^{-1} (Au–S–C bending modes), 390 and 405 cm^{-1} (CH_2 rocking vibrations), 491 cm^{-1} (C–C–S bending modes) and 562 cm^{-1} (C–S stretching modes).

To further investigate the position of the Pd dopant we carried out DFT calculations for isomers of $Pd_2Au_{36}(SC_2H_4Ph)_{24}$ with the two Pd dopants in different positions: in the staples, on the core surface and in the centre. We used the $-SC_2H_4Ph$ for this purpose. The calculations were done with charge 2-in order to preserve the cluster delocalized

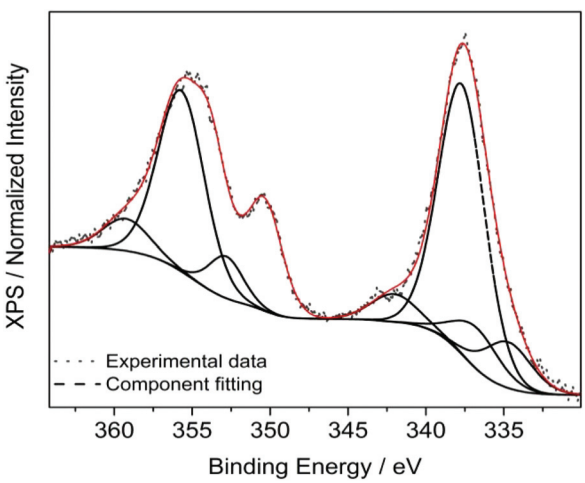

Fig. 2 Au 4d and Pd 3d XP spectra of $Pd_2Au_{36}(SC_2H_4Ph)_{24}$, experimental data are denoted in grey dots, envelop and Shirley background, and component fitting are denoted in black.

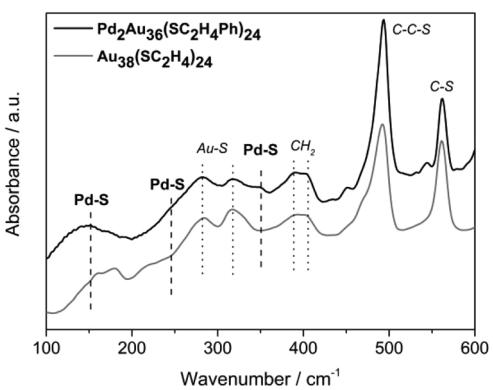

Fig. 3 FIR spectroscopy of $Au_{38}(SC_2H_4Ph)_{24}$ and $Pd_2Au_{36}(SC_2H_4Ph)_{24}$ nanoclusters.

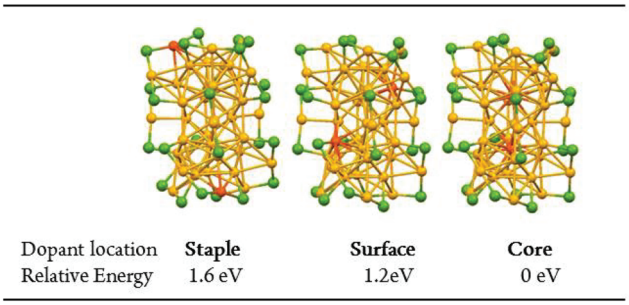

Scheme 1 Optimized structures for $Pd_2Au_{36}(SCH_2CH_2Ph)_{24}$. R group is omitted for the sake of simplicity. Key: red = Pd; yellow = Au; green = S.

electron count of 14, as is the case in $Au_{38}(SR)_{24}$.[65] To facilitate the comparison, we chose three representative models. Scheme 1 shows the optimized structures and corresponding relative energy of three representative models with both the two Pd atoms in the long staples, on the core surface and inside the core. The atomic coordinates of each model are given in ESI.† By considering the relative energy, the core doped structure is unambiguously favoured over the staple and core surface doped structures by the energy differences of 1.6 eV (core–staple) and 1.2 eV (core–surface), which are much beyond the inaccuracy of theory. The features of calculated optical absorption for the three models were compared with the experimental spectrum. Fig. 4a shows the characteristic peaks in experimental UV-vis spectrum of $Pd_2Au_{36}(SC_2H_4Ph)_{24}$ at 418, 535, 616 and 733 nm. A clear difference of absorption spectra feature for the three models can be observed in Fig. 4a, which can be related with different geometry distortion of $Au_{38}(SR)_{24}$ by Pd doping and different electronic structure in the three models.[65] Although the three models show different calculated UV features, none of them gives a perfect fit with the experimental spectra. The calculated spectrum of the staple doped cluster is likely the closest to the experimental spectrum.

For more detailed comparison, we further studied theoretical CD spectra (Fig. 4b), which are more sensitive to the structure. The handedness of $Pd_2Au_{36}(SC_2H_4Ph)_{24}$ E2 can be assigned to be anticlockwise by comparing the calculated with experimental CD spectra. Significant differences between the isomers are observed in the calculated CD spectra. The overall shape and the peak positions of the calculated CD spectra of the core doped structure (Fig. 4b) agrees the best from all the models with the experimental spectra in the bands at 344(+), 386(+), and 607(+) nm taking into account a minor redshift in computed spectrum. The two adjacent minima seen in the experimental spectrum at 431(−) and 474(−) nm do not perfectly match only with the one minimum seen close to 500(−) nm in the calculated CD-spectrum of the core doped model. In that region combining the characteristic features of the spectra from both, staple and core doped models, would give the best agreement. The total energies of two staple doped structures (two Pd dopants in long staples and one Pd dopant in long

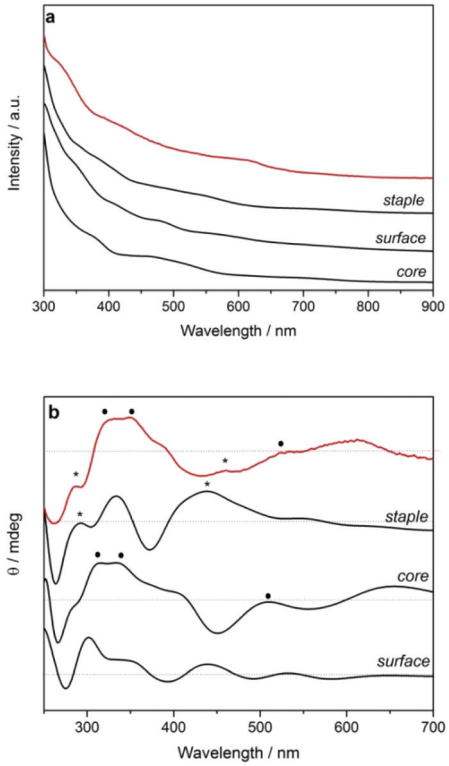

Fig. 4 Comparison between experimental (red) and calculated (black) (a) absorption and (b) CD spectra of $Pd_2Au_{36}(SC_2H_4Ph)_{24}$ nanocluster. Coincident peaks between experimental and theoretical spectra are shown by asterisks (* staple model; ● core model). Calculations were done for three different models (see text for more details).

and one in short staple) are close, as is compared in Scheme S1.† The calculated optical and CD spectra of these structures are quite similar (Fig. S3a, S3b†). We therefore concentrated on the mode with both Pd atoms in long staples.

To summarize, DFT and TDDFT calculations show reasonable UV and CD spectra compared to experiments and do not overrule the possibility for mixed contribution from core-centre and staple Pd doped clusters, although, the core centre doped cluster is energetically the most favourable. The presence of staple doped structure could be explained by the electro-positivity of Pd atom compared to Au atom (2.2 for Pd and 2.4 for Au), which stabilizes the cluster in aerobic preparation and storage condition.[36] However, the exact position of both Pd atoms and the composition of the mixture cannot be determined by this method.

XAFS measurement of the doped cluster was done to study the environment of Pd atoms. The experimental Pd K-edge Fourier transformed EXAFS spectrum of $Pd_2Au_{36}(SC_2H_4Ph)_{24}$ is shown in Fig. 5a. The peak at 1.89 Å corresponds to the Pd–S first coordination shell. The minor peak at 2.80 Å can be assigned to the Pd–Au first coordination shell. The Pd–S peak is clearly evidenced. In addition, the intensity of the Pd–Au peak is much lower than the Pd–S peak, indicating that the staple doped species exist in the $Pd_2Au_{36}(SC_2H_4Ph)_{24}$ sample.

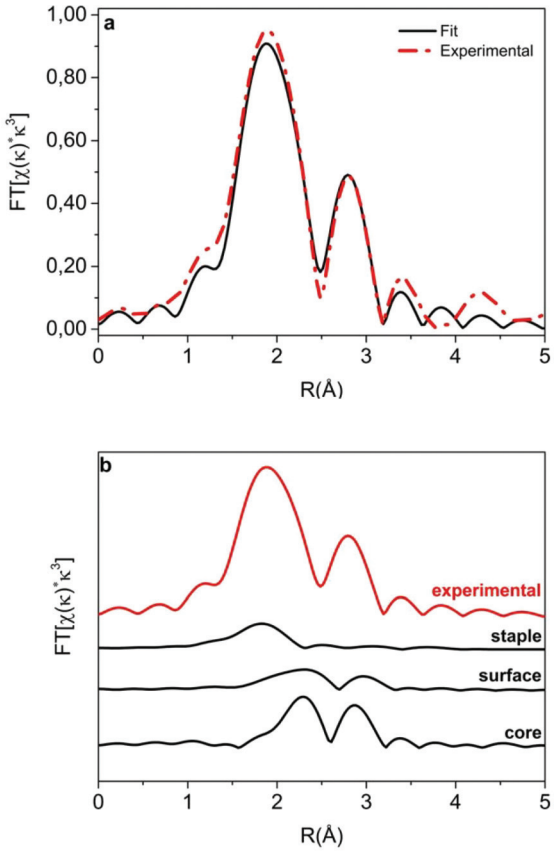

Fig. 5 EXAFS spectra of $Pd_2Au_{36}(SC_2H_4Ph)_{24}$ in R space: (a) experimental and fitted spectra for a mixture of staple and core doped models. (b) Experimental and simulated EXAFS spectra for the staple, surface and core doped models.

Previous studies on dopant location on gold clusters like $PtAu_{24}(SR)_{18}$ [51] and $PdAu_{24}(SR)_{18}$ [47] observed a low intensive peak (around 2 Å in R space), fitting with the distance of Pt–S and Pd–S bonds, respectively. These were assigned to impurities related with noble metal-sulphur oligomers which decrease after size exclusion column purification. In our case, the sample has been purified by several separations steps including size exclusion column and chiral HPLC. The dominant intensity of the Pd–S peak after purification therefore indicates that the peak is related with the sample and not with impurities.

For further component analysis, comparison of EXAFS data was made between the representative models and the experimental result (Fig. 5b). The Pd–S peak in the staple doped model (1.85 Å) and the Pd–Au peak in core doped model (2.86 Å) agree with the corresponding peaks in experimental data. However, we could not get any good fit of our EXAFS data which would show a high molar concentration of the surface doped model (Fig. S5†). Therefore the possibility of surface doped structure in the $Pd_2Au_{36}(SC_2H_4Ph)_{24}$ sample is excluded. To investigate the influence of the Pd dopant location of the staple doped model on the simulated spectra, we compared the simulated FT EXAFS spectra of the models with both Pd atoms in the long staples and short staples structure (Fig. S6†). Almost the same spectra were obtained from the two models. This is due to the fact that the Pd–S distances are similar for short and long staples. EXAFS is therefore not sensitive to the exact location of the Pd dopant within the staple and the structure with both Pd atoms in the long staples was chosen to fit the composition of a mixture of staple and core doped structures. A good fit for the first two shells is shown in Fig. 5a and Table S1.† A composition estimation of 54% staple doped structure and 46% center doped structure was determined. It should be noted however that measurements at room temperature can lead to underestimation of the amount of core doped clusters, as suggested by previous studies.[31,54]

Previous studies on heteroatom doping of $Au_{38}(SR)_{24}$ showed the possibility to dope up to five Ag atoms.[45] However, to the best of our knowledge, in the case of Pd, up to two atoms can be doped into $Au_{38}(SR)_{24}$ whereas only a single Pd atom can be doped into $Au_{25}(SR)_{18}$. Such specific doping behaviour of Pd strongly favours the core-centre model. However the present results show the possibility of staple doping for the $Au_{38}(SR)_{24}$ cluster. Some hypothesis could be considered in order to explain the staple model although experimental verification is still missing. Based on previous work from Tsukuda *et al.*,[36] doping at staple position of Cu in $Au_{25}(SR)_{18}$ was confirmed by EXAFS measurements although this position was computationally less stable. This is ascribed to the lower surface energy of Au (1.55 J m^{-2}) compared to Cu(111) (1.83 J m^{-2}), like it is the case for Pd(111) (2.00 J m^{-2}).

Furthermore, the presence of two doping locations for $Pd_2Au_{36}(SR)_{24}$ could be related with synthesis parameters. During the synthesis the formation of doped $Pd_xAu_y(SR)_m$ and also un-doped Au_{38} was reported. One hypothesis is the direct formation of core doped $Pd_2Au_{36}(SR)_{24}$ and a second doping process of the $Au_{38}(SR)_{24}$ cluster with Pd atoms in the solution, leading to the staple doping. The process of the incorporation of heteroatom to a magic number cluster has been observed before in the case of Ag and $Au_{25}(SR)_{18}$, recently reported.[43] Finally, it should be noted that in previous studies[32] the mixture after the synthesis was aged in THF or in presence of thiol. In contrast, our sample was not aged but was separated by several SEC and HPLC runs.

Conclusions

In conclusion, a combined experimental and theoretical study of the Pd dopant location in $Pd_2Au_{36}(SC_2H_4Ph)_{24}$ nanocluster was done for the first time. The presence of Pd–S bond in the pure cluster is clearly shown in the EXAFS spectra and confirmed by XPS and FIR spectroscopy. The centre doped structure is proved by DFT calculations to be the most stable structure. Comparison of experimental and theoretical optical absorption, CD and EXAFS spectra further suggests a mixture of staple and core doped structures in the sample. However,

the exact position of the two Pd atoms in the staple cannot be determined by the methods applied. The presence of less energetically favoured staple doped structure could be due to its stability against aerobic preparation and storage condition.

Acknowledgements

BZ thanks The China Scholarship Council (No. 201306340012). NB is grateful to The Swiss National Foundation for the Marie Heim-Vögtlin grant (PMPDP2_145512). Support from The Swiss National Science Foundation (grant number 200020_152596 and PP00P2_133482) is acknowledged. JL is Serra Hunter Fellow and grateful to ICREA Academia program. EK kindly acknowledge the funding from Academy of Finland (no. 284562 and 278743).

References

1 H. Hakkinen, *Nat. Chem.*, 2012, **4**, 443–455.
2 S. Knoppe, S. Malola, L. Lehtovaara, T. Burgi and H. Hakkinen, *J. Phys. Chem. A*, 2013, **117**, 10526–10533.
3 A. Das, C. Liu, H. Y. Byun, K. Nobusada, S. Zhao, N. Rosi and R. Jin, *Angew. Chem., Int. Ed.*, 2015, **54**, 3140–3144.
4 Q. Tang, R. Ouyang, Z. Tian and D.-e. Jiang, *Nanoscale*, 2015, **7**, 2225–2229.
5 M. Zhu, C. M. Aikens, F. J. Hollander, G. C. Schatz and R. Jin, *J. Am. Chem. Soc.*, 2008, **130**, 5883–5885.
6 M. W. Heaven, A. Dass, P. S. White, K. M. Holt and R. W. Murray, *J. Am. Chem. Soc.*, 2008, **130**, 3754–3755.
7 H. F. Qian, W. T. Eckenhoff, Y. Zhu, T. Pintauer and R. C. Jin, *J. Am. Chem. Soc.*, 2010, **132**, 8280–8281.
8 S. Knoppe, J. Boudon, I. Dolamic, A. Dass and T. Burgi, *Anal. Chem.*, 2011, **83**, 5056–5061.
9 S. Knoppe, I. Dolamic, A. Dass and T. Bürgi, *Angew. Chem., Int. Ed.*, 2012, **51**, 7589–7591.
10 P. D. Jadzinsky, G. Calero, C. J. Ackerson, D. A. Bushnell and R. D. Kornberg, *Science*, 2007, **318**, 430–433.
11 H. F. Qian and R. C. Jin, *Chem. Mater.*, 2011, **23**, 2209–2217.
12 A. Dass, *J. Am. Chem. Soc.*, 2009, **131**, 11666–11667.
13 P. R. Nimmala and A. Dass, *J. Am. Chem. Soc.*, 2011, **133**, 9175–9177.
14 D. Crasto, S. Malola, G. Brosofsky, A. Dass and H. Hakkinen, *J. Am. Chem. Soc.*, 2014, **136**, 5000–5005.
15 G. Li, C. Zeng and R. Jin, *J. Am. Chem. Soc.*, 2014, **136**, 3673–3679.
16 C. Zeng, H. Qian, T. Li, G. Li, N. L. Rosi, B. Yoon, R. N. Barnett, R. L. Whetten, U. Landman and R. Jin, *Angew. Chem., Int. Ed.*, 2012, **51**, 13114–13118.
17 M. Z. Zhu, H. F. Qian and R. C. Jin, *J. Phys. Chem. Lett.*, 2010, **1**, 1003–1007.
18 Y. Yu, X. Chen, Q. F. Yao, Y. Yu, N. Yan and J. P. Xie, *Chem. Mater.*, 2013, **25**, 946–952.
19 T. Tsukuda and H. Hakkinen, *Protected Metal Clusters: From Fundamentals to Applications*, Elsevier, 2015.
20 R. C. Jin and K. Nobusada, *Nano Res.*, 2014, **7**, 285–300.
21 C. A. Fields-Zinna, M. C. Crowe, A. Dass, J. E. F. Weaver and R. W. Murray, *Langmuir*, 2009, **25**, 7704–7710.
22 K. A. Kacprzak, L. Lehtovaara, J. Akola, O. Lopez-Acevedoa and H. Hakkinen, *Phys. Chem. Chem. Phys.*, 2009, **11**, 7123–7129.
23 Y. Negishi, T. Iwai and M. Ide, *Chem. Commun.*, 2010, **46**, 4713–4715.
24 Y. Negishi, K. Munakata, W. Ohgake and K. Nobusada, *J. Phys. Chem. Lett.*, 2012, **3**, 2209–2214.
25 H. Qian, B. Ellen, Y. Zhu and R. Jin, *Acta Phys. Chim. Sin.*, 2011, **27**, 513–519.
26 H. F. Qian, D. E. Jiang, G. Li, C. Gayathri, A. Das, R. R. Gil and R. C. Jin, *J. Am. Chem. Soc.*, 2012, **134**, 16159–16162.
27 Y. Niihori, W. Kurashige, M. Matsuzaki and Y. Negishi, *Nanoscale*, 2013, **5**, 508–512.
28 A. Tlahuice-Flores, *J. Nanopart. Res.*, 2013, **15**, 1771.
29 H. Yao and R. Kobayashi, *J. Colloid Interface Sci.*, 2014, **419**, 1–8.
30 Y. Negishi, W. Kurashige, Y. Niihori, T. Iwasa and K. Nobusada, *Phys. Chem. Chem. Phys.*, 2010, **12**, 6219–6225.
31 Y. Niihori, M. Matsuzaki, T. Pradeep and Y. Negishi, *J. Am. Chem. Soc.*, 2013, **135**, 4946–4949.
32 Y. Negishi, K. Igarashi, K. Munakata, W. Ohgake and K. Nobusada, *Chem. Commun.*, 2012, **48**, 660–662.
33 N. Barrabes, B. Zhang and T. Burgi, *J. Am. Chem. Soc.*, 2014, **136**, 14361–14364.
34 A. C. Dharmaratne and A. Dass, *Chem. Commun.*, 2014, **50**, 1722–1724.
35 W. Kurashige, K. Munakata, K. Nobusada and Y. Negishi, *Chem. Commun.*, 2013, **49**, 5447–5449.
36 S. Yamazoe, W. Kurashige, K. Nobusada, Y. Negishi and T. Tsukuda, *J. Phys. Chem. C*, 2014, **118**, 25284–25290.
37 C. Kumara, C. M. Aikens and A. Dass, *J. Phys. Chem. Lett.*, 2014, **5**, 461–466.
38 X. Y. Dou, X. Yuan, Y. Yu, Z. T. Luo, Q. F. Yao, D. T. Leong and J. P. Xie, *Nanoscale*, 2014, **6**, 157–161.
39 M. Zhou, Y. Q. Cai, M. G. Zeng, C. Zhang and Y. P. Feng, *Appl. Phys. Lett.*, 2011, **98**, 143103.
40 T. Udayabhaskararao and T. Pradeep, *J. Phys. Chem. Lett.*, 2013, **4**, 1553–1564.
41 H. Y. Yang, Y. Wang, H. Q. Huang, L. Gell, L. Lehtovaara, S. Malola, H. Hakkinen and N. F. Zheng, *Nat. Commun.*, 2013, **4**, 2422.
42 H. Y. Yang, Y. Wang, J. Z. Yan, X. Chen, X. Zhang, H. Hakkinen and N. F. Zheng, *J. Am. Chem. Soc.*, 2014, **136**, 7197–7200.
43 S. Wang, Y. Song, S. Jin, X. Liu, J. Zhang, Y. Pei, X. Meng, M. Chen, P. Li and M. Zhu, *J. Am. Chem. Soc.*, 2015, **137**, 4018–4021.
44 C. Kumara, C. M. Aikens and A. Dass, *J. Phys. Chem. Lett.*, 2014, **5**, 461–466.

45 C. Kumara, K. J. Gagnon and A. Dass, *J. Phys. Chem. Lett.*, 2015, **6**, 1223–1228.
46 A. Tlahuice-Flores, *Phys. Chem. Chem. Phys.*, 2014, **16**, 18083–18087.
47 Y. Negishi, W. Kurashige, Y. Kobayashi, S. Yamazoe, N. Kojima, M. Seto and T. Tsukuda, *J. Phys. Chem. Lett.*, 2013, **4**, 3579–3583.
48 D. M. Chevrier, M. A. MacDonald, A. Chatt, P. Zhang, Z. K. Wu and R. C. Jin, *J. Phys. Chem. C*, 2012, **116**, 25137–25142.
49 T. Dainese, S. Antonello, J. A. Gascon, F. F. Pan, N. V. Perera, M. Ruzzi, A. Venzo, A. Zoleo, K. Rissanen and F. Maran, *ACS Nano*, 2014, **8**, 3904–3912.
50 C. L. Heinecke, T. W. Ni, S. Malola, V. Makinen, O. A. Wong, H. Hakkinen and C. J. Ackerson, *J. Am. Chem. Soc.*, 2012, **134**, 13316–13322.
51 S. L. Christensen, M. A. MacDonald, A. Chatt, P. Zhang, H. F. Qian and R. C. Jin, *J. Phys. Chem. C*, 2012, **116**, 26932–26937.
52 P. Zhang, *J. Phys. Chem. C*, 2014, **118**, 25291–25299.
53 E. Gottlieb, H. Qian and R. Jin, *Chemistry*, 2013, **19**, 4238–4243.
54 I. Dolamic, S. Knoppe, A. Dass and T. Bürgi, *Nat. Commun.*, 2012, **3**, 798.
55 J. J. Mortensen, L. B. Hansen and K. W. Jacobsen, *Phys. Rev. B: Condens. Matter*, 2005, **71**, 035109.
56 J. Enkovaara, C. Rostgaard, J. J. Mortensen, J. Chen, M. Dulak, L. Ferrighi, J. Gavnholt, C. Glinsvad, V. Haikola, H. A. Hansen, H. H. Kristoffersen, M. Kuisma, A. H. Larsen, L. Lehtovaara, M. Ljungberg, O. Lopez-Acevedo, P. G. Moses, J. Ojanen, T. Olsen, V. Petzold, N. A. Romero, J. Stausholm-Moller, M. Strange, G. A. Tritsaris, M. Vanin, M. Walter, B. Hammer, H. Hakkinen, G. K. H. Madsen, R. M. Nieminen, J. Norskov, M. Puska, T. T. Rantala, J. Schiotz, K. S. Thygesen and K. W. Jacobsen, *J. Phys.: Condens. Matter*, 2010, **22**, 253202.
57 J. P. Perdew and Y. Wang, *Phys. Rev. B: Condens. Matter*, 1992, **45**, 13244–13249.
58 M. J. Casida, C. Jamorski, F. Bohr, J. Guan and D. R. Salahub, *Theoretical and Computational Modeling of NLO and Electronic Materials*, ACS Press, Washington, D.C., 1996.
59 M. Walter, H. Hakkinen, L. Lehtovaara, M. Puska, J. Enkovaara, C. Rostgaard and J. J. Mortensen, *J. Chem. Phys.*, 2008, **128**, 244101.
60 J. P. Perdew, K. Burke and M. Ernzerhof, *Phys. Rev. Lett.*, 1996, **77**, 3865–3868.
61 B. Ravel and M. Newville, *J. Synchrotron Radiat.*, 2005, **12**, 537–541.
62 J. B. Tracy, M. C. Crowe, J. F. Parker, O. Hampe, C. A. Fields-Zinna, A. Dass and R. W. Murray, *J. Am. Chem. Soc.*, 2007, **129**, 16209–16215.
63 I. Dolamic, B. Varnholt and T. Burgi, *Phys. Chem. Chem. Phys.*, 2013, **15**, 19561–19565.
64 E. D. Risberg, J. Mink, A. Abbasi, M. Y. Skripkin, L. Hajba, P. Lindqvist-Reis, E. Bencze and M. Sandstrom, *Dalton Trans.*, 2009, 1328–1338, DOI: 10.1039/B814252A.
65 B. Molina, A. Sanchez-Castillo, S. Knoppe, I. L. Garzon, T. Burgi and A. Tlahuice-Flores, *Nanoscale*, 2013, **5**, 10956–10962.